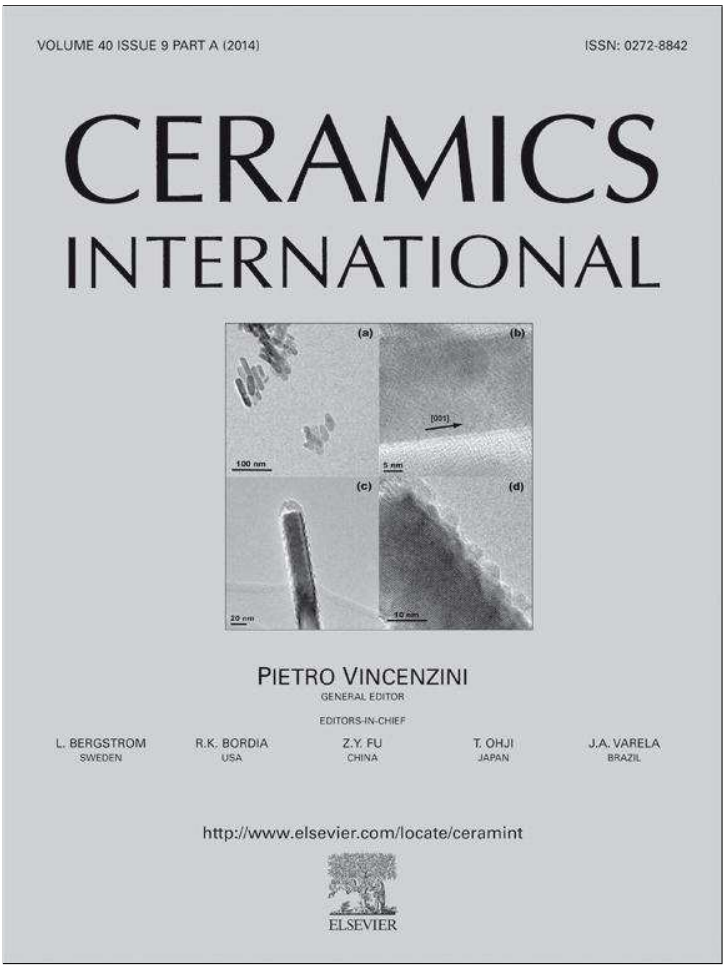

Available online at www.sciencedirect.com

ScienceDirect

Ceramics International 40 (2014) 14413–14419

CERAMICS INTERNATIONAL

www.elsevier.com/locate/ceramint

Copper substitution effect on the structural properties of nickel ferrites

A. Rais[a,*], K. Taibi[b], A. Addou[c], A. Zanoun[d], Y. Al-Douri[e]

[a]*Laboratoire de Physico-Chimie des Matériaux Avancés, Université Djilali Liabes, Sidi Bel Abbes 22000, Algeria*
[b]*Laboratory of Materials Science and Engineering, USTHB, Algiers, Algéria*
[c]*Laboratoire des Sciences et Techniques de l'Environnement et de la Valorisation, Faculté des Sciences et de la technologie, Université de Mostaganem, Algeria*
[d]*Department of Physics and Chemistry, ENSET of Oran, Algeria*
[e]*Institute of Nanoelectronic Engineering, University of Malaysia Perlis, 01000 Kangar, Malaysia*

Received 25 March 2014; received in revised form 5 June 2014; accepted 6 June 2014
Available online 16 June 2014

Abstract

Nickel–copper ferrites with the general formula $Ni_{1-x}Cu_xFe_2O_4$ ($0 \le x \le 1$) were studied using X-ray diffraction and infrared absorption spectroscopy. XRD diffraction patterns show that all samples have a pure single-phase cubic spinel structure over the whole composition range. From these patterns, the lattice parameters, crystallite size and porosity of these samples have been calculated and compared with those predicted theoretically. Most of the values were found to increase with increasing Cu content. Far infrared absorption spectra show high and low absorption bands corresponding to tetrahedral and octahedral sites confirming the single phase spinnel structure. The calculated force constants, K_t and K_o for the two sites are found to increase with increasing Cu content and their relative values are consistent with bond length magnitudes at tetrahedral and octahedral sites.

Keywords: D. Spinel; Ni–Cu ferrites; XRD; IR; SEM

1. Introduction

Mixed ferrites are widely used for many kind of industrial applications such as information storage systems, high frequency microwave devices and transformers because of their singular electrical and magnetic properties. Various substitutions in these materials have been incorporated to achieve the desired characteristics and investigations have been focused on Ni–Cu mixed spinel ferrite because copper containing ferrites have interesting structural, electrical and magnetic properties [1–7].

The application of IR spectroscopy to the ferrite materials can be used to observe the achievement of the solid-state reaction as well as the purity of the spinel structure phase. IR spectra provide important information on the deformation of the spinel structure and various ordering problems [8,9]. Furthermore, the concentration variation of metal cations in some mixed ferrites may produce structural changes within the unit cell without affecting the spinel structure as a whole. These structural changes brought by the metal cations that are either lighter or heavier than other metal ions in the ferrites strongly influence the lattice vibration. The IR spectra absorption bands mainly appear due to the vibrations of the oxygen ions with the cations producing various frequencies of the unit cell [10]. Note also that the vibration frequency depends on the cations-oxygen distance, the bonding force and the cations mass [11].

The study of cations distribution at octahedral and tetrahedral position is essential for industrial applications of copper–nickel ferrites. As far as we are aware, no structural and IR study of the completely Cu-substituted Ni ferrites have been reported. The present work is concerned mainly with the analysis of experimental result of X-ray diffraction and infrared spectra in $Ni_{1-x}Cu_xFe_2O_4$ over the whole composition range from $x=0$ to $x=1$.

2. Experimental

The conventional double sintering technique was used to prepare samples of $Ni_{1-x}Cu_xFe_2O_4$ ($x=0$–1 step 0,1). The ingredient materials were analytical high purity grade $NiCO_3$,

*Corresponding author. Tel./fax: +213 771 244 466.
E-mail address: amrais@yahoo.com (A. Rais).

http://dx.doi.org/10.1016/j.ceramint.2014.06.037
0272-8842/

Fe_2O_3 and CuO (BDH). They were weighed stoichiometrically as per chemical formula unit. They were mixed thoroughly in an agate mortar to produce a homogeneous mixture of fine particles; the process of mixing was carried out in slurry of acetone to ensure uniformity. Pellets of 10 mm and 3–5 mm thick are prepared using a hydraulic press at 4 tons/cm^2. These pellets were first sintered at 1000 °C for 12 h in air medium followed by cooling at room temperature. The pre-sintered samples were ground then remixed once more and reshaped in the hydraulic press to pellets. These, were finally re-sintered at 1100 °C for 24 h followed by natural cooling. The sample compositions were confirmed by energy dispersive X-ray spectroscopy (EDS) analysis. The single-phase spinel structure was confirmed by the X-ray diffraction spectrum of these samples obtained with a Panalytical X'Pert Pro diffractometer using CuKα radiation (λ = 1.540598 Å). Scan's range was kept the same for all samples $2\theta = 20–100^\circ$ using a step size of 0.01° with sample time of 10 s.

For recording IR spectra, samples were prepared by mixing small quantity of the powdered ferrites with KBr. Then, the samples mixed powder was pressed in a cylindrical disc at 10 tons/cm^2 by hydraulic press. The IR measurements of the prepared samples were recorded at room temperature in the range from 200 cm^{-1} up to 1000 cm^{-1} using Perkin-Elmer 783 FT-IR spectrophotometer. The microstructure and sample morphology were examined with analytical scanning electron microscope (ASEM) JEOL; JSM6360. The ASEM is coupled with an energy dispersive system (EDS, EDAX) for elementary composition analysis of samples.

3. Results and discussion

Specimen spectra of X-ray diffraction for the $Ni_{1-x}Cu_xFe_2O_4$ samples at compositions of $x = 0$; 0.2; 0.5; 0.8 and 1 are shown in Fig. 1. As can be seen, the XRD patterns present peaks at reflection planes indexed (220), (311), (222), (400), (422), (511), (440), (620), (533) and (553) for all samples, thus proving the formation of the single phase cubic spinel structure. The lattice parameters a_{exp} for all samples have been calculated using the Nelson–Riley extrapolation method [12]. Values of a_{exp} are tabulated in Table 1 and their variations with Cu content are shown in Fig. 2. Values of the lattice parameter a_{exp} for $NiFe_2O_4$ and $CuFe_2O_4$ samples have been found equal to 8.331 and 8.407 Å, respectively, which agrees reasonably well with the literature values for $NiFe_2O_4$ [13,14] and for $CuFe_2O_4$ [7,14]. The bigger a_{exp} value for $CuFe_2O_4$ compared with that of $NiFe_2O_4$ is due to the larger ionic radius of Cu^{2+} (0.72 Å) than both Fe^{3+} (0.67 Å) and Ni^{2+} (0.69 Å). The increasing trend with Cu content is attributed to the replacement of smaller Fe^{3+} ions by a larger ionic radius of the Cu^{2+} at the tetrahedral sites (A), and the replacement of the Ni^{2+} ions by a smaller ionic radius Fe^{3+} at the octahedral sites [B]. The non-linear behavior of a_{exp} with Cu content was reported for other similar ferrites systems passing from partially to completely inverse spinel type structure [15]. Nickel ferrite, $NiFe_2O_4$ has totally inverse

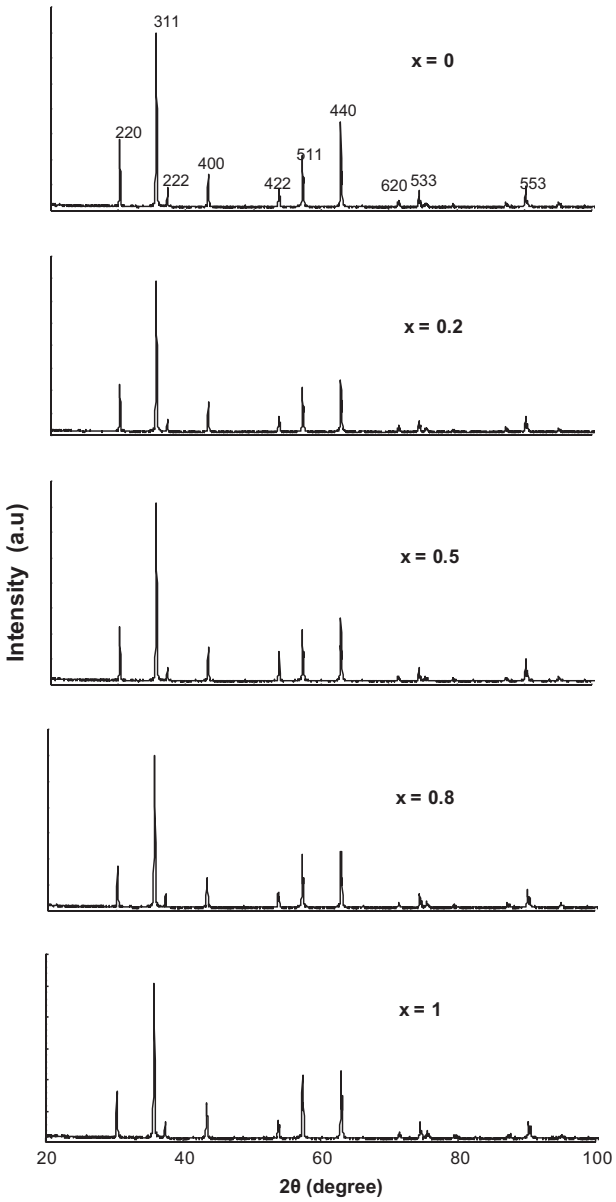

Fig. 1. The X-ray diffraction pattern for $Ni_{1-x}Cu_xFe_2O_4$ of samples $x = 0$, 0.2, 0.5, 0.8, 1.

spinel structure with half of the Fe^{3+} ions in B sites and the other half in A sites and all the Ni^{2+} ions in octahedral sites [13]. Copper ferrite, $CuFe_2O_4$ is partially an inverse spinel and the degree of inversion depends upon heat treatment [7,16]. In the $Ni_{1-x}Cu_xFe_2O_4$ ferrites the Ni^{2+} ions exclusively occupy the octahedral sites [17], while some of the Cu^{2+} ions prefer to occupy the tetrahedral sites and the rest are stable in the octahedral sites [13]. Thus, the cations distribution for $Ni_{1-x}Cu_xFe_2O_4$ ferrites can be written as [18]

$$(Cu^{2+}{}_{fi}Fe^{3+}{}_{1-fi})[Ni^{2+}{}_{1-x}Cu^{2+}{}_{x-fi}Fe^{3+}{}_{1+fi}]O^{2-}{}_4 \text{ with } 0 \le x \le 1 \quad (1)$$

Where the factor of inversion fi can be taken as: $0.05 \le fi \le 0.1$

Table 1
Lattice parameters a_{exp} and a_{th}, cation radius at (A) and [B] sites, r_A and r_B, cation distributions of $Ni_{1-x}Cu_xFe_2O_4$ ferrites.

x	a_{exp} (Å) ± 0.001	a_{th} (Å)	r_A (Å)	r_B (Å)	Cation distributions [Refs. [7, 13, 14, 16, 17]]
0	8.331	8.650	0.6727	0.6786	$(Fe^{3+}_{1-0,05})^A[Ni^{2+}_{1-0}\ Fe^{3+}_{1+0,05}]^B$
0.1	8.336	8.655	0.673	0.680	$(Cu^{2+}_{0,06}Fe^{3+}_{1-0,06})^A[Ni^{2+}_{1-0.1}\ Cu^{2+}_{0.1-0,06}\ Fe^{3+}_{1,06}]^B$
0.2	8.342	8.659	0.6732	0.6818	$(Cu^{2+}_{0,06}Fe^{3+}_{1-0,06})^A[Ni^{2+}_{1-0,2}\ Cu^{2+}_{0,2-0,06}\ Fe^{3+}_{1,06}]^B$
0.3	8.348	8.664	0.6735	0.6832	$(Cu^{2+}_{0,07}Fe^{3+}_{1-0,07})^A[Ni^{2+}_{1-0,3}\ Cu^{2+}_{0,3-0,07}\ Fe^{3+}_{1,07}]^B$
0.4	8.353	8.669	0.6737	0.6845	$(Cu^{2+}_{0,07}Fe^{3+}_{1-0,07})^A[Ni^{2+}_{1-0.4}\ Cu^{2+}_{0.4-0,07}\ Fe^{3+}_{1,07}]^B$
0.5	8.359	8.673	0.6741	0.6863	$(Cu^{2+}_{0,08}Fe^{3+}_{1-0,08})^A[Ni^{2+}_{1-0,5}\ Cu^{2+}_{0,5-0,08}\ Fe^{3+}_{1,08}]^B$
0.6	8.364	8.678	0.6744	0.688	$(Cu^{2+}_{0,08}Fe^{3+}_{1-0,08})^A[Ni^{2+}_{1-0,6}\ Cu^{2+}_{0,6-0,08}\ Fe^{3+}_{1,08}]^B$
0.7	8.371	8.683	0.6745	0.690	$(Cu^{2+}_{0,09}Fe^{3+}_{1-0,09})^A[Ni^{2+}_{1-0.7}\ Cu^{2+}_{0.7-0,09}\ Fe^{3+}_{1,09}]^B$
0.8	8.379	8.687	0.6749	0.6918	$(Cu^{2+}_{0,09}Fe^{3+}_{1-0,09})^A[Ni^{2+}_{1-0,8}\ Cu^{2+}_{0,8-0,09}\ Fe^{3+}_{1,09}]^B$
0.9	8.391	8.692	0.675	0.693	$(Cu^{2+}_{0.1}\ Fe^{3+}_{1-0.1})^A[Ni^{2+}_{1-0.9}\ Cu^{2+}_{0.9-0.1}\ Fe^{3+}_{1.1}]^B$
1	8.407	8.696	0.6754	0.6943	$(Cu^{2+}_{0.1}\ Fe^{3+}_{1-0.1})^A[\ Cu^{2+}_{1-0.1}\ Fe^{3+}_{1.1}]^B$

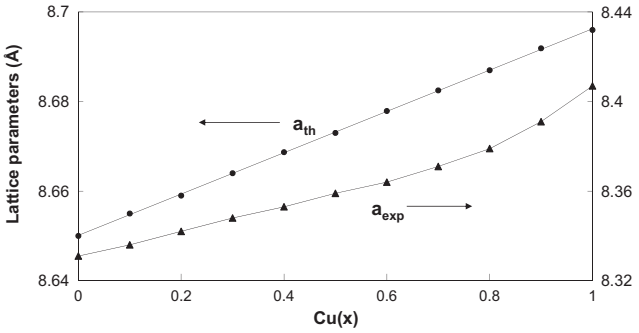

Fig. 2. Lattice parameters *aexp* and *ath* as the function of Cu(*x*).

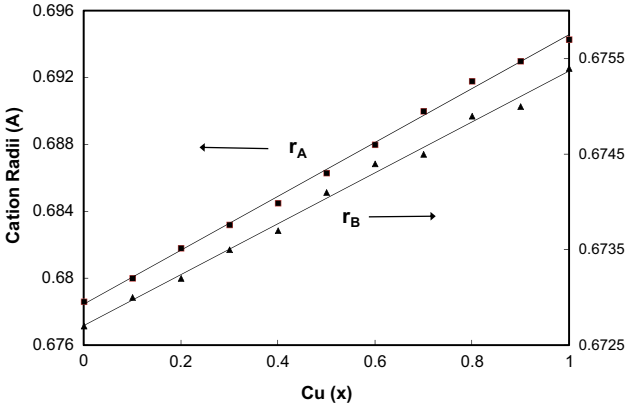

Fig. 3. Cation radii, r_A and r_B as the function of Cu(*x*).

Given this cations distribution, the average cation radius at the A and B sites, r_A and r_B can be calculated for all samples using the relations [19]:

$$r_A = fir_{Cu} + (1-fi)r_{Fe} \tag{2}$$

$$r_B = [(1-x)r_{Ni} + (x-fi)r_{Cu} + (1+fi)r_{Fe}]/2 \tag{3}$$

where r_{Ni}, r_{Cu} and r_{Fe} are the ionic radii of Ni^{2+}, Cu^{2+} and Fe^{3+} ions, respectively.

The theoretical lattice parameter can be calculated using the following relation between the average cation radius of the constituents at different sites [20]

$$a_{th} = \frac{8}{3\sqrt{3}}\left[r_A + R_o + \sqrt{3}(r_B + R_o)\right] \tag{4}$$

where R_o (=1.38 Å) is the radius of the oxygen ion. Table 1 shows a_{exp}, the calculated a_{th}, r_A, r_B and the cation distributions. Fig. 2 shows the variation of experimental and theoretical lattice parameter with Cu ions content. As can be seen, a_{exp} is smaller than a_{th}, this is because the theoretical value assumes a perfectly filled spinnel structure where anions and cations are taken as plain spheres. Similar behavior has been seen in Li–Mn ferrites [20]. Fig. 3 shows clearly that values of r_A and r_B increase with increasing Cu^{2+} ions content, we can interpret this to the replacement of Fe^{3+} ions with larger ionic radius of the Cu^{2+}, at both the tetrahedral and octahedral sites. Similar results have been reported for Co–Cd [15] ferrites.

The inter-ionic cations–anions distances (bond lengths) at A-sites, R_A, and B-sites, R_B can be evaluated using the relations [21]

$$R_A = a\sqrt{3}\left(\delta + \frac{1}{8}\right) \tag{5}$$

$$R_B = a\sqrt{3\delta^2 - \frac{\delta}{2} + \frac{1}{16}} \tag{6}$$

$$\delta = \mathrm{U} - 0.375 \tag{7}$$

$$U = \frac{(r_A + R_o)}{a\sqrt{3}} + \frac{1}{4} \tag{8}$$

where U represents the oxygen positional parameter and δ represents the deviation from the ideal value U_{ideal} (=0.375). Values of U, R_A and R_B are shown in Table 3. It is clear that the bond length of A-site R_A is less than that of B-site R_B. In addition, both lengths show an increasing trend with Cu content. This may be attributed to the increase of the lattice

Table 2
Edge lengths R_X, $R_{X'}$ and $R_{X''}$, bulk and XRD densities d_{exp}, d_X, porosity P and crystallite size L as the function of Cu(x).

x	R_X (Å)	$R_{X'}$ (Å)	$R_{X''}$ (Å)	d_{exp} (g/cm^3) ±0.01	d_X (g/cm^3)	P (%)	L (nm) ±1
0	3.356	2.535	2.960	4.41	5.357	17.7	143
0.1	3.356	2.538	2.961	4.46	5.362	16.8	124
0.2	3.353	2.542	2.963	4.50	5.368	16.2	146
0.3	3.357	2.545	2.965	4.53	5.373	15.7	115
0.4	3.3572	2.548	2.967	4.54	5.378	15.6	150
0.5	3.358	2.552	2.969	4.55	5.383	15.5	123
0.6	3.358	2.555	2.971	4.56	5.390	15.3	133
0.7	3.359	2.560	2.973	4.58	5.395	15.1	101
0.8	3.359	2.565	2.976	4.60	5.399	14.7	121
0.9	3.359	2.573	2.979	4.66	5.405	13.8	116
1	3.360	2.584	2.985	4.72	5.409	12.7	162

Table 3
Lattice parameter a_{exp}, oxygen parameter U, bond lengths at (A) and [B] sites R_A and R_B, band frequencies ν_1, ν_2 and force constants K_t and K_o as the function of Cu(x).

x	a_{exp} (Å) ±0.001	U	R_A (Å)	R_B (Å)	ν_1 (cm^{-1})	ν_2 (cm^{-1})	$K_t \times 10^5$ (dyne/cm)	$K_o \times 10^5$ (dyne/cm)
0	8.331	0.3942	1.890	2.034	580	400	2.315	1.045
0.1	8.336	0.3924	1.891	2.035	583	400	2.320	1.045
0.2	8.342	0.3923	1.893	2.037	585	405	2.324	1.035
0.3	8.348	0.3922	1.894	2.038	587	400	2.335	1.045
0.4	8.353	0.3921	1.895	2.039	590	397	2.343	1.096
0.5	8.359	0.3920	1.897	2.041	592	395	2.346	1.124
0.6	8.364	0.3920	1.898	2.042	595	393	2.350	1.135
0.7	8.371	0.3919	1.899	2.044	597	392	2.355	1.140
0.8	8.379	0.3918	1.901	2.046	598	390	2.358	1.144
0.9	8.391	0.3916	1.904	2.049	600	390	2.360	1.144
1	8.407	0.3913	1.908	2.053	600	390	2.360	1.144

parameter due to replacement of nickel ions by bigger size copper ions.

The tetrahedral edge length R_X, the shared octahedral length $R_{X'}$ and the unshared octahedral length $R_{X''}$ of these cubic mixed spinel oxides have been calculated using the following equations [22]:

$$R_X = a\sqrt{2}(2U-0.5) \tag{9}$$

$$R_{X'} = a\sqrt{2}(1-2U) \tag{10}$$

$$R_{X''} = a\sqrt{4U^2-3U+\frac{11}{16}} \tag{11}$$

Values of R_X, $R_{X'}$ and $R_{X''}$ are shown in Table 2. All three edge lengths show an increasing trend with Cu content certainly for the same reasons as R_A and R_B. Moreover, it is interesting to note that the largest values are those of the tetrahedral edge lengths R_X and the smallest are those of the shared octahedral edge lengths $R_{X'}$ for all concentrations Cu(x).

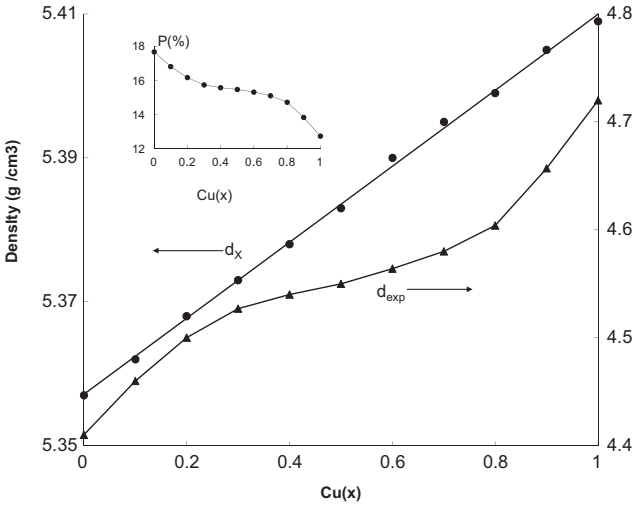

Fig. 4. Densities dX and $dexp$ as the function of Cu(x). Inset: Porosity P as the function of Cu(x).

The X-ray density d_X for each sample is calculated according to the relation [12]

$$d_X = \frac{ZM}{Na^3} \tag{12}$$

where Z, M, N and a^3 represent the number of molecules per unit cell (=8), molecular weight, Avogadro's number and volume of the unit cell, respectively. The bulk densities d_{exp} (=mass/volume) of the sample were measured using a pycnometer. Values of the calculated d_X and measured d_{exp} are shown in Table 2 and plotted in Fig. 4 as function of Cu content. d_X increases linearly while d_{exp} increases non-linearly with Cu content. These trends support the variation in the lattice parameters. The true density, d_X, is higher than the bulk density d_{exp} for all samples. This is due to the existence of pores appearing during the preparation. Hence, the porosity P (%), can be calculated using the following relation:

$$P = 1 - \frac{d_{exp}}{d_X} \tag{13}$$

The variation of the porosity P with Cu content is shown in the inset of Fig. 4 and appears to decrease non-linearly with Cu content between about 18% and 13%. Similar values of P and behavior have been reported for Ni–Co ferrites [23].

The average crystallite size, L, of all samples was evaluated from the reflected diffraction peaks using Scherrer's equation [12]:

$$L = \frac{k\lambda}{\beta \cos\theta} \tag{14}$$

where the constant k=0.89, λ is the wavelength of the X-ray radiation (=1.540598 Å), θ is the diffraction angle of the most intense peak (311) and β is its full width at half maximum (FWHM) in radian. Values of the crystallite size are given in Table 2. The average value of L was observed to be 130 nm. Comparable results have been reported for Ni–Cr ferrites [17].

The analysis of the results of the scanning electron microscope (SEM) coupled with EDS and the observations with

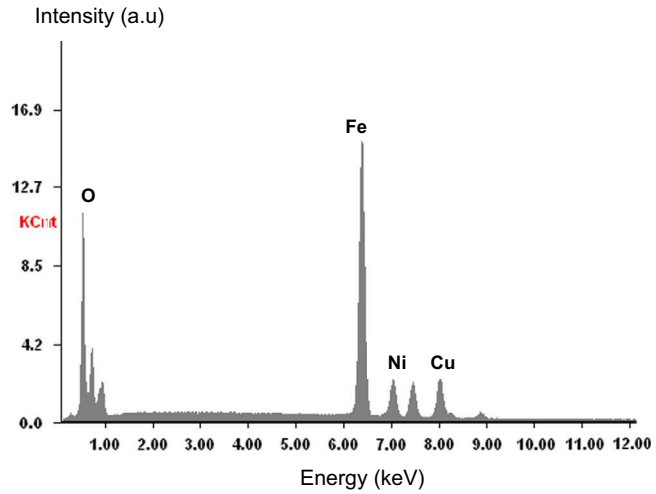

Fig. 5. EDS pattern of sample $x=0.5$ for qualitative and quantitative element analysis.

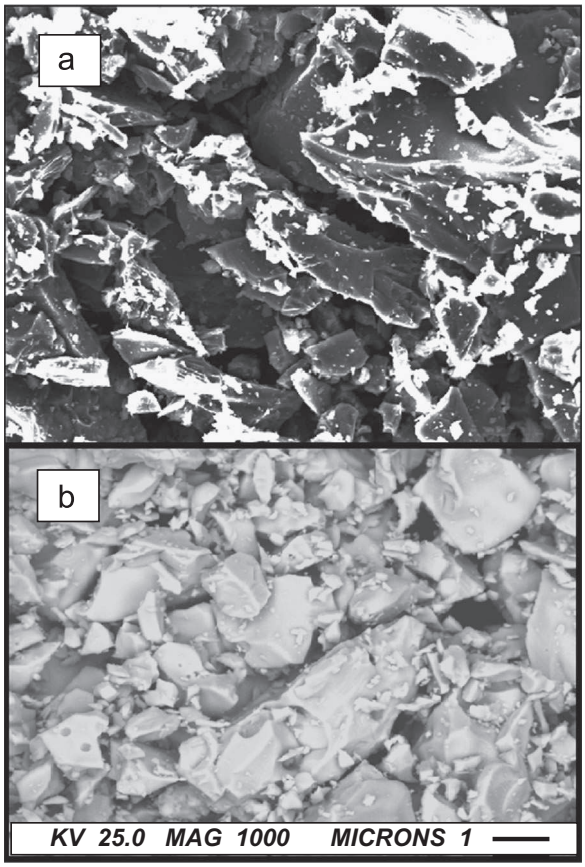

Fig. 6. SEM micrograph of ferrites Ni_{1-x} Cu_x Fe_2 O_4 samples: (a) $x=1$: Secondary electron (SE) image in morphological contrast mode. (b) $x=0$: backscattered electron (BSE) image in compositional contrast mode.

backscattered electron images confirm well the samples purity. A representative EDS graph in Fig. 5 for sample of Cu content $x=0.5$ shows a homogeneous composition of the expected stoichiometry. The SEM micrographs of Fig. 6 (a) and (b) are in morphological and compositional modes for sample

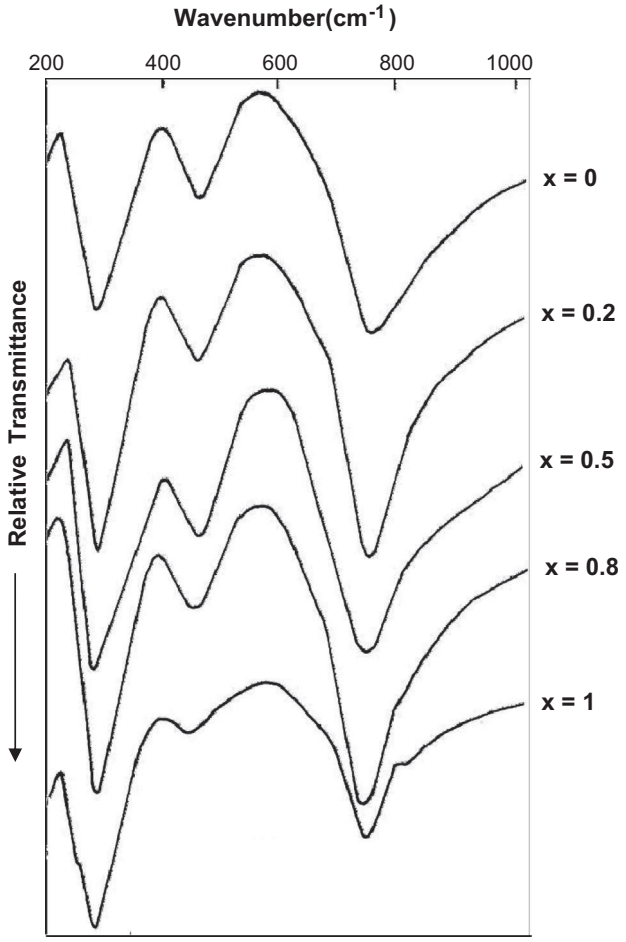

Fig. 7. IR spectra for Ni_{1-x} Cu_x Fe_2 O_4 of samples $x=0$, 0.2, 0.5, 0.8, 1.

compositions $x=1$ and $x=0$ respectively. Both images show well packed and continuous grain structure with pores and small holes at the grain boundaries. It can be observed from secondary electrons image of Fig. 6 (a) that most of the pores are within the grains and not on the boundaries. The existence of pores is consistent with our porosity calculations using densities d_{exp} and d_X (Table 2).

The infrared spectra measurements of the $Ni_{1-x}Cu_xFe_2O_4$ in the range 200–1000–1000 cm^{-1} indicate the presence of two strong absorption bands ν_1 (580–600 cm^{-1}) and ν_2 (400–390 cm^{-1}). Fig. 7 shows the typical IR spectra of $Ni_{1-x}Cu_x$-Fe_2O_4 ferrites. The band positions are listed in Table 3 as the function of Cu content. The observed absorption bands within this limit reveal and confirm the formation of single-phase spinel structure having two sublattices: tetrahedral (A) site and octahedral (B) site [11]. The absorption band ν_1 observed around 580 cm^{-1} is attributed to the stretching vibration mode of metal–oxygen in the tetrahedral sites, whereas ν_2 observed around 400 cm^{-1} is assigned to octahedral group complexes. The difference in the position of the two strong bonds can be related to the differences in the Fe–O bond lengths at A-sites and B-sites. It is clear that the Fe–O bond length at A-sites (1.890–1.908 Å) is shorter than that of the B-sites (2.034–2.053 Å). Clearly, this effect can be interpreted as due to more

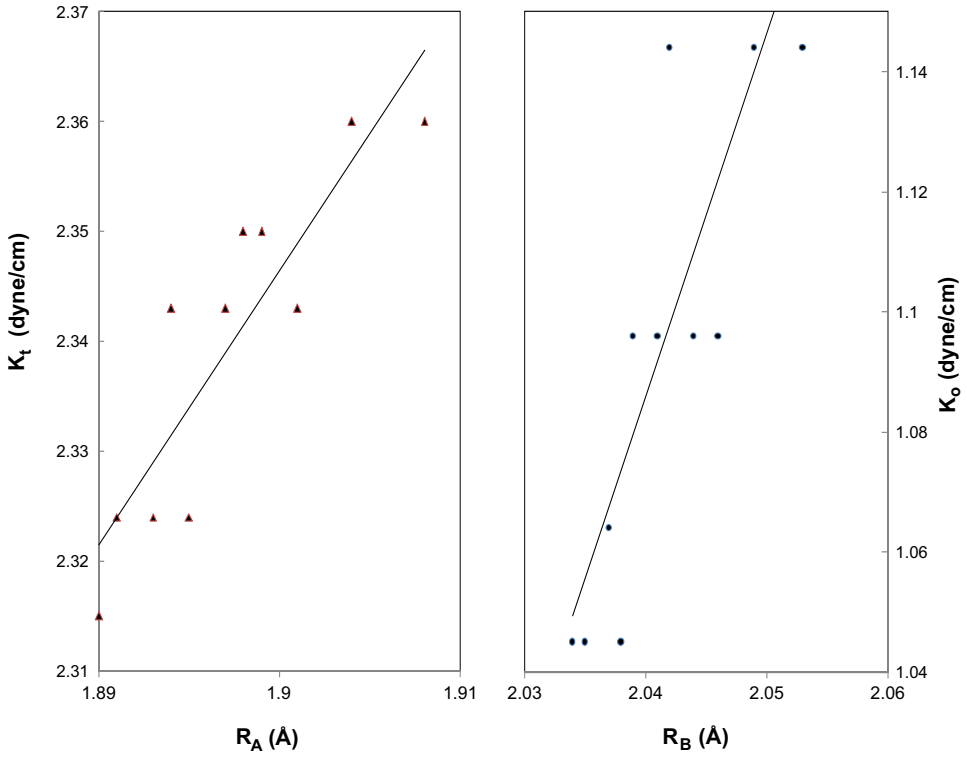

Fig. 8. Force constants K_t and K_o versus bond lengths R_A and R_B.

covalent bonding on A-sites than that on B-sites [24]. The wave number of the first band ν_1, increases with Cu content, while ν_2 decreases with Cu content. These variations can be attributed to the effects of increasing bond lengths of both sites with Cu content and the stretching of the lattice parameter as Cu^{2+} replaces Fe^{3+} in B-sites and partially in A-sites. This indicates the strengthening of the metal–oxygen bonds at the octahedral sites due to the shifts of more Fe ions from A-sites to B-sites. These results agree to some extent with results of Ni–Al [19].

The force constants of the ions at the tetrahedral site (K_t) and octahedral site (K_o) have been calculated using the IR band frequencies ν_1 and ν_2 in the following formula [25]:

$$K_{t/o} = 4\pi^2 c^2 \nu_{1/2}^2 \mu \quad (15)$$

where c is the light speed ($\approx 2.99 \times 10^{10}$ cm/s), ν is the vibration frequency of the A- and B- sites and μ is the reduced mass of the Fe^{3+} and O^{2-} ions. Table 3 shows variation of K_t and K_o with Cu content. It can be seen that the trend of both K_t and K_o is increasing with Cu content. One may interpret this behavior as due to the increase in bond lengths of both A and B-sites, R_A and R_B with Cu content. Moreover, for a given concentration x, shorter bond length R_A has larger force constant K_t, possibly because breaking long bond length requires less energy than breaking short bond length. The variation of force constants K_t and K_o with the corresponding bond lengths R_A and R_B, respectively, is shown in Fig. 8. According to Srivastava and Srinivasan [26] the band stretching for tetrahedral sites would lead to higher force constant than that of band stretching for the octahedral site. From Fig. 8, it can be seen that the magnitude of K_t is higher than K_o and that the force constants K_t and K_o increase with the increasing bond lengths. Similar results have been reported for the Cu–Zn system [9]. Since for a given x, the increase in bond length tends to decrease the force constant, one may attribute this to the fact that oxygen can form under favorable conditions, strong bonds with the metal ions even at large inter-ionic separations. Similar behavior has been reported for other metal oxides like Cu–Zn–Cr [27] and Li–Mg–Zn [8].

4. Conclusion

The characterization of Ni_{1-x} Cu_x Fe_2 O_4 ferrites system prepared by the conventional solid state reaction with double sintering around 1000 °C shows that

1. The crystalline structure is a pure single phase cubic spinel over the whole composition range from $x=0$ to $x=1$.
2. The measured lattice constant a_{exp} increases non-linearly with increasing Cu(x) content, thus deviating a bit from Vegard's law.
3. The theoretical lattice a_{th}, cation radius and bond length at A and B sites calculated on the basis of proposed cations distribution show the same trend. Values of a_{exp} agree reasonably well with a_{th}.
4. The IR spectra indicate two main absorption bands, a high band (580–600 cm^{-1}) for tetrahedral (A) sites and a lower band (390–400 cm^{-1}) for octahedral [B] sites, thus confirming the single phase spinel structure.

5. The calculated force constants, K_t and K_o for the two sites are found to increase with increasing Cu content. In addition, for a given concentration x, K_t is larger than K_o. This is consistent with the bond length magnitudes at A and B sites.

Acknowledgment

One of us (A. Rais) would like to thank Prof. M. Belbachir for useful comments.

References

[1] N. Rezlescu, E. Rezlascu, Abnormal dielectric behaviour of copper containing ferrites, Solid State Commun. 14 (69) (1974).
[2] N. Rezlescu, E. Rezlescu, Dielectric properties of copper containing ferrites, Phys. Status Solidi A 23 (1974) 575.
[3] N. Nanba, S. Kobayashi, Semiconductive Properties and Cation Distribution of Copper Ferrites$Cu_{1-\delta}Fe_{2+\delta}O_4$, Jpn. J. Appl. Phys. 17 (819) (1978).
[4] K.P. Belov, A.N. Goryaga, L.L. Antoshina, Anomalous electrical resistivity in the region of compensation temperature in ferrites $NiFe_{1.26}V_{0.74}\cdot O_4$, Sov. Phys. Solid State 16 (1975) 1596.
[5] A.A. Ghani, A.I. Eatah, A.A. Mohamed, in: H. Watanabe, S. Iida, M. Sugimoto (Eds.), Ferrites: Proceedings of the ICF 3, Center for Acad. Pub., Japan, Tokyo, 1980, p. 324.
[6] S.R. Sawant, R.N. Patil, Magnetic hysteresis studies on slow cooled and quenched $Cu_xZn_{1-x}Fe_2O_4$system, Solid State Commun. 40 (1981) 391.
[7] A.D. Al-Rawas, A. Rais, A.A. Yousif, A.M. Gismelseed, M.E. Elzain, S. Mazen, A. Al-Falaky, Magnetic properties of $Cu_{1+x}M_xFe_{2-2x}O_4$ mixed ferrites (M=Ge,Ti), J. Magn. Magn. Mater. 269 (2004) 168.
[8] A.M. Shaikh, S.A. Jadhav, S.C. Watawe, B.K. Chongnle, Infrared spectral studies of Zn-substituted Li–Mg ferrites, Mater. Lett. 44 (2000) 192.
[9] T.T. Srinivasan, C.M. Srivastava, N. Venkataramani, M.J. Patni, Far-infrared spectra for copper–zinc mixed ferrites, Bull. Mater. Sci. 6 (1984) 1063.
[10] A.M. Sankpal, S.R. Sawant, A.S. Vaingankar, Relaxation time studies on $Ni_{0.7}Zn_{0.3}Al_xFe_{2-x}O_4$ and $Ni_{0.7}Zn_{0.3}Cr_xFe_{2-x}O_4$, Ind. J. Pure Appl. Phys. 26 (1988) 459.
[11] R.D. Waldron, Infrared spectral studies in spinnel structure ferrites, Phys. Rev. 99 (1955) 1727.
[12] B.D Cullity, Elements of X-Ray Diffraction, Addison-Wesley Publishing Company, Inc, USA, 1978, p. 338.
[13] A. Rais, A.M. Gismelseed, I.A. Al-Omari, Cation distribution and magnetic properties of nickel–chromium ferrites $NiCr_x\ Fe_{2-x}\ O_4$, Phys. Status Solidi B 242 (2006) 1497–1503.
[14] S. Manjura Hoque, Md. Amanullah Choudhury, Md. Fakhrul Islam, Characterization of Ni–Cu mixed spinel ferrite, J. Magn. Magn. Mater 251 (2002) 292–303.
[15] A.M. Abdeena, O.M. Hemedaa, E.E. Assem, M.M. El-Sehlya, Structural, electrical and transport phenomena of Co ferrite substituted by Cd, J. Magn. Magn. Mater 238 (2002) 75–83.
[16] H.M Zaki, Structure, analysis and some magnetic properties for low temperature fired Ni–Cu ferrite, Physica B 407 (2012) 2025–2031.
[17] M.A. Gabal, Y.M. Al Angari, Effect of chromium ion substitution on the electromagnetic properties of nickel ferrite, Mater. Chem. Phys. 118 (2009) 153–160.
[18] H. Knoch, H. Dannheim, Temperature dependence of cation distribution in magnesium ferrite, Phys. Status Solidi A 37 (1976) K135.
[19] A.G. Bhosale, B.K. Chougule: X-ray, infrared and magnetic studies of Al-substituted Ni ferrites Mater. Chem.Phys. 97, 273-276 (2006).
[20] S.A. Mazen n, N.I. Abu-Elsaad, Structural and some magnetic properties of manganese substituted lithium ferrites, J. Magn. Magn. Mater. 324 (2012) 3366–3373.
[21] K.J. Standley, Oxide Magnetic Materials, Claredon Press, Oxford, 1990.
[22] C. Otero Arean, E. Garcia Diaz, J.M. Rubio Gonzalez, M.A. Villa Garcia, Crystal chemistry of cadmium–zinc ferrites, J. Solid State Chem. 77 (1988) 275.
[23] R.C. Kambale, P.A. Shaikh, S.S. Kamble, Y.D. Kolekar, Effect of cobalt substitution on structural, magnetic and electric properties of nickel ferrite, J. Alloys Compd. 478 (2009) 599–603.
[24] B. Evans, S. Hanfner, Mössbauer resonance of Fe^{57} in oxidic spinels containing Cu and Fe, J. Phys. Chem. Solids 29 (1573) (1968).
[25] P.A. Shaikh, R.C. Kambale, A.V. Rao, Y.D. Kolekar, Structural, magnetic and electrical properties of Co–Ni–Mn ferrites, J. Alloys Compd. 492 (2010) 590.
[26] C.M. Srivastava, T.T. Srinivasan,and, R Aivar, Exchange constants in ferrimagnetic garnets, J. Appl. Phys. 53 (1982) 781.
[27] M.A. Ahmed, N. Okasha, Role of Cu^{2+} concentration on the structure and transport properties of Cr–Zn ferrites, J. Magn. Magn. Mater. 321 (2009) 3436–3441.